Monthly Notices
of the
ROYAL ASTRONOMICAL SOCIETY

MNRAS **466,** 1542–1554 (2017)
Advance Access publication 2016 November 30

doi:10.1093/mnras/stw3094

Studying stellar spin-down with Zeeman–Doppler magnetograms

V. See,[1,2★] M. Jardine,[1] A. A. Vidotto,[3] J.-F. Donati,[4,5] S. Boro Saikia,[6] R. Fares,[7] C. P. Folsom,[4,5,8,9] É. M. Hébrard,[10] S. V. Jeffers,[6] S. C. Marsden,[11] J. Morin,[12] P. Petit,[4,5] I. A. Waite[11] and the BCool Collaboration

[1]*SUPA, School of Physics and Astronomy, University of St Andrews, North Haugh, KY16 9SS St Andrews, UK*
[2]*Department of Physics and Astronomy, University of Exeter, Physics Building, Stocker Road, Exeter EX4 4QL, UK*
[3]*School of Physics, Trinity College Dublin, University of Dublin, Dublin-2, Ireland*
[4]*Université de Toulouse, UPS-OMP, Institut de Recherche en Astrophysique et Planétologie, F-31400 Toulouse, France*
[5]*CNRS, Institut de Recherche en Astrophysique et Planétologie, 14 Avenue Edouard Belin, F-31400 Toulouse, France*
[6]*Universität Göttingen, Institut für Astrophysik, Friedrich-Hund-Platz 1, D-37077 Göttingen, Germany*
[7]*INAF – Osservatorio Astrofisico di Catania, Via Santa Sofia, 78, I-95123 Catania, Italy*
[8]*Univ. Grenoble Alpes, IPAG, F-38000 Grenoble, France*
[9]*CNRS, IPAG, F-38000 Grenoble, France*
[10]*Department of Physics and Astronomy, York University, Toronto, ON M3J 1P3, Canada*
[11]*Computational Engineering and Science Research Centre, University of Southern Queensland, Toowoomba, QLD 4350, Australia*
[12]*Laboratoire Univers et Particules de Montpellier, Université de Montpellier, CNRS, F-34095, France*

Accepted 2016 November 25. Received 2016 November 24; in original form 2016 September 16

ABSTRACT

Magnetic activity and rotation are known to be intimately linked for low-mass stars. Understanding rotation evolution over the stellar lifetime is therefore an important goal within stellar astrophysics. In recent years, there has been increased focus on how the complexity of the stellar magnetic field affects the rate of angular-momentum loss from a star. This is a topic that Zeeman–Doppler imaging (ZDI), a technique that is capable of reconstructing the large-scale magnetic field topology of a star, can uniquely address. Using a potential field source surface model, we estimate the open flux, mass-loss rate and angular-momentum-loss rates for a sample of 66 stars that have been mapped with ZDI. We show that the open flux of a star is predominantly determined by the dipolar component of its magnetic field for our choice of source surface radius. We also show that, on the main sequence, the open flux, mass-loss and angular-momentum-loss rates increase with decreasing Rossby number. The exception to this rule is stars less massive than $0.3\,M_{\odot}$. Previous work suggests that low-mass M dwarfs may possess either strong, ordered and dipolar fields or weak and complex fields. This range of field strengths results in a large spread of angular-momentum-loss rates for these stars and has important consequences for their spin-down behaviour. Additionally, our models do not predict a transition in the mass-loss rates at the so-called wind-dividing line noted from Lyα studies.

Key words: techniques: polarimetric – stars: activity – stars: evolution – stars: magnetic field – stars: rotation.

1 INTRODUCTION

Studies of open clusters at different ages show that the rotation periods of low-mass stars ($0.1\,M_{\odot} \lesssim M_{\star} \lesssim 1.4\,M_{\odot}$) evolve coherently as a function of mass and age (Barnes 2003, 2010; Irwin & Bouvier 2009; Meibom et al. 2011, 2015; Barnes et al. 2016; Stauffer et al. 2016). While no complete theory currently exists to explain how rotation periods evolve over the stellar lifetime, a number of processes have been identified as being integral to any such theory. On the pre-main sequence, angular-momentum conservation causes stars to spin-up as they contract. However, star–disc interactions appear to prevent stars reaching the break-up speeds expected from contraction alone (Koenigl 1991; Rebull, Wolff & Strom 2004; Matt et al. 2010, 2012a). Along the main sequence, stars spin-down as a result of stellar winds that carry away angular momentum (Weber & Davis 1967). Additionally, transport processes redistribute angular momentum within the star and can lead to core–envelope decoupling (MacGregor & Brenner 1991; Allain 1998; Bouvier 2008; Spada et al. 2011), adding a further layer of complexity to the problem.

Studying the mass-loss rates of low-mass stars and their associated spin-down torques is a non-trivial task because of the

★ E-mail: w.see@exeter.ac.uk

diffuse nature of stellar winds. For example, the Sun has a mass-loss rate of $\sim 10^{-14}\,\mathrm{M}_{\odot}\,\mathrm{yr}^{-1}$ resulting in a wind number density of only $\sim 5\,\mathrm{cm}^{-3}$ in the vicinity of Earth (Balikhin, Gedalin & Petrukovich 1993). With the key exception of indirect mass-loss rate estimates from Lyα observations (see Wood et al. 2014 and references therein), the majority of work has been theoretical by necessity.

A number of complementary approaches exist in the literature for tackling the rotation evolution problem. One approach involves using multidimensional magnetohydrodynamic (MHD) simulations to determine the mass-loss rates and spin-down torques of individual stars. These can incorporate realistic magnetic field geometries at the stellar surface to give improved estimates over simulations that use idealized field geometries (Vidotto et al. 2012, 2014a; Alvarado-Gómez et al. 2016; Nicholson et al. 2016). Another approach involves deriving braking laws that predict the spin-down torque as a function of fundamental stellar parameters (e.g. Matt et al. 2012b; Cohen & Drake 2014; Réville et al. 2015a). These braking laws can then be incorporated into rotation evolution models, with the aim of reproducing the rotation-period distributions observed in open clusters at different ages (Reiners & Mohanty 2012; Gallet & Bouvier 2013, 2015; van Saders & Pinsonneault 2013; Brown 2014; Johnstone et al. 2015; Matt et al. 2015; Amard et al. 2016; Blackman & Owen 2016; van Saders et al. 2016).

Studies have shown that a key parameter for determining the stellar spin-down torque is the open flux (Mestel & Spruit 1987; Vidotto et al. 2014a; Réville et al. 2015a,b), i.e. the flux contained in wind bearing field lines that extend away from the star. However, rotation evolution models typically only incorporate the surface magnetic field strength into their braking laws. This is partly driven by the lack of systematic studies of how open flux varies with fundamental stellar parameters. By doing so, these models neglect the topology of the magnetic fields and their effects on the rate of mass-loss and angular-momentum loss (Garraffo, Drake & Cohen 2015).

One way of estimating the open flux of the star is by using a field extrapolation model (e.g. Jardine, Collier Cameron & Donati 2002) in conjunction with a magnetogram obtained via Zeeman–Doppler imaging (ZDI). ZDI is a tomographic imaging technique that can reconstruct the large-scale component of stellar magnetic fields at the stellar surface (Semel 1989; Brown et al. 1991; Donati & Brown 1997; Donati et al. 2006). Previous work has already shown that fundamental stellar parameters such as internal structure (Donati et al. 2008; Morin et al. 2008b, 2010; Donati & Landstreet 2009; Gregory et al. 2012), rotation period (Petit et al. 2008; See et al. 2015b, 2016) and age (Vidotto et al. 2014b; Folsom et al. 2016; Rosén et al. 2016) can affect the surface magnetic field topologies of cool stars. We will build on these previous works and investigate how parameters such as open flux, mass-loss rates and angular-momentum-loss rates vary with fundamental stellar parameters such as mass or rotation.

In Section 2, we outline the characteristics of the sample used in this study and the wind model we employ. In Section 3, we discuss how the open flux, mass-loss rate and angular-momentum-loss rate vary across our sample. Additionally, we also compare our results to those obtained from 3D MHD simulations. Concluding remarks follow in Section 4.

2 SAMPLE AND WIND MODEL

In this work, we use a sample of 66 stars that have each been mapped with ZDI. Many of these stars have been mapped over multiple epochs resulting in a total of 106 ZDI maps used in this work. The sample of stars used in this study is mostly comprised of the sample used by See et al. (2015b).[1] However, the sample has been expanded to include more stars presented by Folsom et al. (2016), Hébrard et al. (2016) and Hébrard et al (in preparation). To date, this is the largest sample of ZDI maps used in a single study and represents well over a decade of effort observing and reconstructing the surface magnetic fields of main-sequence cool dwarfs. The stars within the sample were observed under numerous programmes including a large fraction from the BCool (Marsden et al. 2014) and Toupies (Folsom et al. 2016) collaborations. In Table 1, we list the physical parameters of each star used in this study. Stellar masses, radii and rotation periods are taken from Vidotto et al. (2014b) or the paper in which each ZDI map was originally published. The Rossby number is given by the rotation period divided by the convective turnover time, $\mathrm{Ro} = P_{\mathrm{rot}}/\tau_{\mathrm{c}}$. In this work, we will use the empirical prescription of Wright et al. (2011, their equation 11) to estimate the convective turnover times for our sample. The reference for the original publication of each ZDI map is also listed in Table 1. The masses and rotation periods of the sample are shown in Fig. 1 (this is an updated version of fig. 1 from See et al. 2015b).

2.1 Magnetic field extrapolation

Using a potential field source surface (PFSS) approach (Altschuler & Newkirk 1969), the 3D magnetic field structure of a star can be determined. This technique has been used in numerous previous works to investigate the structure of stellar coronae (e.g. Jardine et al. 2002; Gregory et al. 2006; Lang et al. 2012; Johnstone et al. 2014). By assuming that the magnetic field is in a potential state, $\underline{\nabla} \times \underline{\boldsymbol{B}} = 0$, it can be defined in terms of a scalar potential, $\underline{\boldsymbol{B}} = -\underline{\nabla}\psi$. Substituting into Gauss' law for magnetism, $\underline{\nabla} \cdot \underline{\boldsymbol{B}} = 0$, we find that the scalar potential is the solution to Laplace's equation, $\nabla^2\psi = 0$. The three components of the magnetic field can therefore be expressed as a sum over spherical harmonics in terms of the associated Legendre polynomials, P_{lm}, as follows:

$$B_r = -\sum_{l=1}^{N}\sum_{m=1}^{l}\left[l a_{lm} r^{l-1} - (l+1)\, b_{lm} r^{-(l+2)}\right] P_{lm}(\cos\theta)\, \mathrm{e}^{im\phi} \quad (1)$$

$$B_\theta = -\sum_{l=1}^{N}\sum_{m=1}^{l}\left[a_{lm} r^{l-1} + b_{lm} r^{-(l+2)}\right] \frac{\mathrm{d}}{\mathrm{d}\theta} P_{lm}(\cos\theta)\, \mathrm{e}^{im\phi} \quad (2)$$

$$B_\phi = -\sum_{l=1}^{N}\sum_{m=1}^{l}\left[a_{lm} r^{l-1} + b_{lm} r^{-(l+2)}\right] P_{lm}(\cos\theta)\, \frac{im}{\sin\theta} \mathrm{e}^{im\phi}. \quad (3)$$

Here, l indicates the spherical harmonic degree and m indicates the order or 'azimuthal number'. a_{lm} and b_{lm} are the amplitudes of each spherical harmonic component. In order to determine the values of a_{lm} and b_{lm}, two boundary conditions are imposed: one at the stellar surface, $r_\star$, and one at the source surface, r_{ss}. The stellar surface boundary is set using a ZDI map. At the source surface, the magnetic field is forced to be purely radial, i.e. $B_\theta = B_\phi = 0$. Physically, the source surface is the location beyond which all field lines are open and carrying a wind. It therefore represents the limit of coronal confinement. In this work, we set the source surface radii to be

[1] Our sample includes a number of stars initially presented by Folsom et al. (2016). These stars were also included in the samples used by Vidotto et al. (2014b) and See et al. (2015b). However, the masses and radii used in those works were preliminary values. We have used the updated values for these stars in this work.

Table 1. Parameters for our sample: stellar mass, radius, rotation period, Rossby number, open flux, average unsigned dipolar field strength at the stellar surface, mass-loss rate, angular-momentum-loss rates for the M12 and R15 formulations, instantaneous spin-down time-scale and the observation epoch. References indicate the paper where the original magnetic map was published.

Star ID	$M_\star$ ($M_\odot$)	$r_\star$ ($r_\odot$)	$P_{\rm rot}$ (d)	Ro	$\Phi_{\rm open}$ (10^{22} Mx)	$\langle\lvert B_{\rm dip}\rvert\rangle$ (G)	$\dot{M}$ ($10^{-12}\,M_\odot\,{\rm yr}^{-1}$)	$\dot{J}_{\rm M12}$ (10^{32} erg)	$\dot{J}_{\rm R15}$ (10^{32} erg)	$\tau_{\rm R15}$ (Gyr)	Obs epoch	Ref.
Solar-like stars												
HD 3651	0.88	0.88	43.4	2.491	5.57	3.65	0.15	0.03	0.02	14.8	–	1
HD 9986	1.02	1.04	23	1.639	1.45	0.69	0.04	0.01	0.01	125	–	1
HD 10476	0.82	0.82	16	0.831	2.41	1.83	0.08	0.02	0.02	52	–	1
κ Ceti	1.03	0.95	9.3	0.673	19.6	10.9	0.66	0.86	0.9	1.94	2012 Oct	2
ϵ Eri	0.86	0.77	10.3	0.572	17.1	14.9	0.44	0.45	0.5	2.76	2007 Jan	3
–	–	–	–	–	11.5	9.9	0.34	0.27	0.28	5	2008 Jan	3
–	–	–	–	–	7.4	6.15	0.32	0.17	0.16	8.81	2010 Jan	3
–	–	–	–	–	10.3	8.93	0.34	0.25	0.24	5.73	2011 Oct	3
–	–	–	–	–	12.5	10.7	0.4	0.32	0.33	4.21	2012 Oct	3
–	–	–	–	–	22.8	19.8	0.58	0.67	0.79	1.74	2013 Oct	3
HD 39587	1.03	1.05	4.8	0.349	12.2	5.57	0.77	1.36	1.09	3.08	–	1
HD 56124	1.03	1.01	18	1.302	4.81	2.42	0.13	0.06	0.05	18.9	–	1
HD 72905	1	1	5	0.346	8.98	4.26	0.6	0.78	0.63	5.02	–	1
HD 73350	1.04	0.98	12.3	0.902	7.8	3.93	0.45	0.24	0.19	6.83	–	1
HD 75332	1.21	1.24	4.8	0.445	20.5	6.84	0.61	2.28	2.12	1.73	–	1
HD 76151	1.24	0.98	20.5	1.975	6.51	3.48	0.2	0.08	0.06	13.5	2007 Jan	4
HD 78366	1.34	1.03	11.4	1.245	19.6	9.36	0.82	0.85	0.81	2.03	–	1
HD 101501	0.85	0.9	17.6	0.962	12.7	7.82	0.37	0.22	0.23	3.54	–	1
ξ Boo A	0.85	0.84	5.6	0.304	34.5	25.1	1.08	2.81	3.36	0.75	–	1
–	–	–	–	–	7.69	5.26	0.51	0.47	0.39	6.48	2008 Feb	5
–	–	–	–	–	15.4	10.5	0.81	1.12	1.11	2.29	2009 July	5
–	–	–	–	–	12.6	9.08	0.74	0.93	0.83	3.05	2010 Jan	5
–	–	–	–	–	22.9	16.6	0.99	1.86	1.96	1.3	2010 Jun	5
–	–	–	–	–	19.3	14	0.78	1.41	1.44	1.76	2010 Jul	5
–	–	–	–	–	24.9	18.1	0.69	1.63	1.88	1.35	2011 Feb	5
ξ Boo B	0.72	1.07	10.3	0.448	28.4	12.4	0.98	1.7	1.89	0.63	–	1
18 Sco	0.98	1.02	22.7	1.524	1.92	0.91	0.07	0.01	0.01	69.9	2007 Aug	4
HD 166435	1.04	0.99	3.4	0.252	9.28	4.29	0.64	1.12	0.93	5.12	–	1
HD 175726	1.06	1.06	3.9	0.296	10.7	4.78	0.55	1.22	0.99	4.27	–	1
HD 190771	0.96	0.98	8.8	0.573	12.7	6.61	0.39	0.49	0.48	3.65	–	1
61 Cyg A	0.66	0.62	34.2	1.327	2.42	3.2	0.06	0.01	0.01	59.8	–	1
HN Peg	1.085	1.04	4.6	0.364	34	15.9	1.19	4.37	4.7	0.79	–	1
–	–	–	–	–	26.6	12.5	0.82	2.86	3	1.21	2007 Jul	6
–	–	–	–	–	13	6.13	0.44	1.08	0.97	3.74	2008 Aug	6
–	–	–	–	–	19.1	9.09	0.6	1.81	1.77	2.05	2009 Jun	6
–	–	–	–	–	23.7	11.3	0.83	2.63	2.62	1.39	2010 Jul	6
–	–	–	–	–	20.3	9.43	0.8	2.2	2.12	1.72	2011 Jul	6
–	–	–	–	–	35.5	16.9	1.09	4.36	4.77	0.76	2013 Jul	6
Young Suns												
AB Dor	1	1	0.5	0.035	150	77.5	9.03	269	256	0.12	2001 Dec	7
–	–	–	–	–	194	99.1	6.91	286	318	0.1	2002 Dec	7
BD-16351	0.9	0.88	3.2	0.19	63.7	42.2	2.21	12.7	16	0.29	2012 Sept	8
DX Leo	0.9	0.81	5.4	0.319	34.3	26.8	0.97	2.55	3.13	0.88	2014 May	8
HII 296	0.9	0.93	2.6	0.155	110	65.6	3.81	36.1	48.1	0.12	2009 Oct	8
HII 739	1.15	1.07	1.6	0.135	18.4	8.13	0.8	5.3	4.34	2.51	2009 Oct	8
HIP 12545	0.95	1.07	4.8	0.31	178	79.6	7.19	52.1	73.3	0.04	2012 Sept	8
HIP 76768	0.8	0.85	3.7	0.186	109	77.7	3.28	21.8	31.9	0.11	2013 May	8
LO Peg	0.75	0.66	0.4	0.019	81.9	97	4.22	84.5	90.2	0.33	2014 Aug	8
PELS 031	0.95	1.05	2.5	0.16	22	9.94	1.29	5.53	4.86	1.26	2013 Nov	8
PW And	0.85	0.78	1.8	0.096	89.6	75.3	3.14	31.2	41.9	0.19	2014 Sept	8
TYC 0486-4943-1.c	0.75	0.69	3.8	0.172	17.2	18.2	0.68	1.35	1.47	2.31	2013 Jun	8
TYC 5164-567-1.c	0.9	0.89	4.7	0.277	98.2	63.8	2.69	14.7	21.3	0.15	2013 Jun	8
TYC 6349-0200-1.c	0.85	0.96	3.4	0.186	69.1	38.5	2.15	14.3	18.2	0.23	2013 Jun	8
TYC 6878-0195-1.c	1.17	1.37	5.7	0.501	137	37.7	4.78	37.2	46.5	0.07	2013 jun	8
V439 And	0.95	0.92	6.2	0.4	18.7	11.4	0.62	1.19	1.21	2.03	2014 Sept	8
V447 Lac	0.9	0.81	4.4	0.262	11.6	8.51	0.66	0.92	0.85	3.94	–	8
Hot Jupiter hosts												
τ Boo	1.34	1.42	3	0.328	2.99	0.72	0.22	0.4	0.21	29.6	2008 Jan	9
–	–	–	–	–	3.31	0.81	0.27	0.5	0.26	24.2	2008 Jun	9
–	–	–	–	–	2.13	0.49	0.16	0.24	0.12	51.2	2008 Jul	9

Table 1 – *continued*

Star ID	$M_\star$ ($M_\odot$)	$r_\star$ ($r_\odot$)	$P_{\rm rot}$ (d)	Ro	$\Phi_{\rm open}$ (10^{22} Mx)	$\langle\lvert B_{\rm dip}\rvert\rangle$ (G)	$\dot{M}$ (10^{-12} $M_\odot$ yr^{-1})	$\dot{J}_{\rm M12}$ (10^{32} erg)	$\dot{J}_{\rm R15}$ (10^{32} erg)	$\tau_{\rm R15}$ (Gyr)	Obs epoch	Ref.
–	–	–	–	–	4.45	1.11	0.24	0.61	0.35	17.6	2009 May	10
–	–	–	–	–	5	1.25	0.36	0.86	0.48	12.9	2010 Jan	10
–	–	–	–	–	5.72	1.45	0.25	0.8	0.5	12.5	2011 Jan	10
HD 46375	0.97	0.86	42	2.777	3.51	2.44	0.09	0.01	0.01	36.1	2008 Jan	10
HD 73256	1.05	0.89	14	1.042	5.59	3.42	0.22	0.09	0.08	15.1	2008 Jan	10
HD 102195	0.87	0.82	12.3	0.695	7.19	5.46	0.25	0.14	0.12	9.47	2008 Jan	10
HD 130322	0.79	0.83	26.1	1.288	2.87	2.12	0.08	0.02	0.01	40.6	2008 Jan	10
HD 179949	1.21	1.19	7.6	0.704	1.73	0.48	0.12	0.05	0.03	67.7	2007 Jun	11
–	–	–	–	–	5.53	1.97	0.24	0.26	0.19	12.4	2009 Sept	11
HD 189733	0.82	0.76	12.5	0.649	4.46	2.76	0.34	0.07	0.07	15.5	2007 Jun	12
–	–	–	–	–	6.01	5.03	0.32	0.12	0.1	10.9	2008 Jul	12
M dwarf stars												
CE Boo	0.48	0.43	14.7	0.387	45.9	128	1.55	0.78	1.24	0.43	2008 Jan	13
DS Leo	0.58	0.52	14	0.461	17.3	32.7	0.62	0.26	0.32	2.22	2007 Jan	13
–	–	–	–	–	12.2	22.2	0.44	0.15	0.18	3.92	2007 Dec	13
GJ 182	0.75	0.82	4.3	0.2	104	78.9	3.59	18.1	26.6	0.11	2007 Jan	13
GJ 49	0.57	0.51	18.6	0.6	10.1	19.8	0.27	0.07	0.09	5.88	2007 Jul	13
AD Leo	0.42	0.38	2.2	0.051	57.1	204	3.36	8.23	12.7	0.23	2007 Jan	14
–	–	–	–	–	58.4	209	2.87	7.68	12.3	0.23	2008 Jan	14
DT Vir	0.59	0.53	2.9	0.096	33.8	61.3	1.18	3.25	4.48	0.79	2007 Jan	13
–	–	–	–	–	10.5	8.83	1.38	0.66	1.11	3.17	2007 Dec	13
EQ Peg A	0.39	0.35	1.1	0.022	87.8	369	2.52	18.9	36	0.15	2006 Aug	14
EQ Peg B	0.25	0.25	0.4	0.006	61.1	505	1.75	18.8	35.3	0.22	2006 Aug	14
EV Lac	0.32	0.3	4.4	0.075	103	588	3.45	5.56	11.8	0.08	2006 Aug	14
–	–	–	–	–	94.8	542	3.04	4.83	10.2	0.1	2007 July	14
DX Cnc	0.1	0.11	0.5	0.004	2.47	104	0.06	0.07	0.11	15.3	2007	15
–	–	–	–	–	1.23	49.8	0.04	0.03	0.04	43.9	2008	15
–	–	–	–	–	1.48	62.7	0.04	0.03	0.05	33.8	2009	15
GJ 1156	0.14	0.16	0.5	0.004	2.26	44.6	0.1	0.12	0.14	18.6	2007	15
–	–	–	–	–	4.67	92	0.16	0.28	0.41	6.44	2008	15
–	–	–	–	–	3.85	76.3	0.13	0.21	0.3	8.86	2009	15
GJ 1245B	0.12	0.14	0.7	0.006	6.34	164	0.16	0.23	0.41	3.52	2006	15
–	–	–	–	–	1.93	50	0.07	0.05	0.07	20.6	2008	15
OT Ser	0.55	0.49	3.4	0.105	38.7	82.1	1.67	3.43	4.82	0.56	2008 Feb	13
V 374 Peg	0.28	0.28	0.5	0.007	107	698	2.79	39.8	81.6	0.1	2005 Aug	16
–	–	–	–	–	94.4	616	2.46	33.3	66.9	0.12	2006 Aug	16
WX Uma	0.1	0.12	0.8	0.006	30.5	1090	1.07	2.06	4.91	0.2	2006	15
–	–	–	–	–	40.4	1449	1.39	3.07	7.7	0.13	2007	15
–	–	–	–	–	40.4	1446	1.3	2.95	7.52	0.13	2008	15
–	–	–	–	–	59.7	2137	1.61	4.69	13.2	0.08	2009	15
YZ Cmi	0.32	0.29	2.8	0.048	115	707	4.15	10.3	22	0.07	2007 Jan	14
–	–	–	–	–	110	675	4.09	9.79	20.6	0.08	2008 Jan	13
GJ 176	0.49	0.47	39.3	1.059	3.62	7.26	0.15	0.01	0.01	22.6	2013 Oct	17
GJ 205	0.63	0.55	33.6	1.229	11.3	19.1	0.29	0.05	0.06	5.31	2013 Oct	18
GJ 358	0.42	0.41	25.4	0.575	43.4	133	1.11	0.34	0.58	0.44	2014 Jan	18
GJ 479	0.43	0.42	24	0.559	11.5	33.3	0.29	0.05	0.07	3.82	2014 Apr	18
GJ 674	0.35	0.4	35.2	0.66	33.5	108	0.85	0.17	0.29	0.5	2014 May	17
GJ 846	0.6	0.54	10.7	0.369	5.31	9.39	0.14	0.05	0.06	17.1	2013 Sept	18
–	–	–	–	–	10.9	19.1	0.29	0.15	0.18	5.29	2014 June	18

1: Petit et al. (in preparation); 2: do Nascimento et al. (2014); 3: Jeffers et al. (2014); 4: Petit et al. (2008); 5: Morgenthaler et al. (2011); 6: Boro Saikia et al. (2015); 7: Donati et al. (2003); 8: Folsom et al. (2016); 9: Fares et al. (2009); 10: Fares et al. (2013); 11: Fares et al. (2012); 12: Fares et al. (2010); 13: Donati et al. (2008); 14: Morin et al. (2008b); 15: Morin et al. (2010); 16: Morin et al. (2008a); 17: Hébrard et al. (in preparation); 18: Hébrard et al. (2016).

$r_{\rm ss} = 3.41 r_\star$ for the entire sample in line with previous studies (Fares et al. 2010, 2012; See et al. 2015a). It is important to note that this is a simplifying assumption and that one should expect the source surface radii to vary with the fundamental parameters of a star (Réville et al. 2015b). Indeed, to properly calculate the source surface radius, one should account for the thermal coronal energy, the bulk kinetic energy of the wind and the magnetic field energy. MHD simulations are able to self-consistently model the interactions between these components (see Section 3.4 for further comparison between our models and multidimensional MHD models). It is therefore possible to estimate effective source surface radii from MHD simulations. Results indicate that the source surface varies by a factor of only a few (e.g. Vidotto et al. 2014a). The choice of a constant source surface radii is therefore a reasonable assumption, at least for this initial work. We will discuss the qualitative effects of varying the source surface radii in Section 3.3.2 leaving detailed exploration of the effect of varying $r_{\rm ss}$ for future work. Equations (1)–(3) apply only between $r_\star$ and $r_{\rm ss}$. Beyond $r_{\rm ss}$, the field remains purely radial

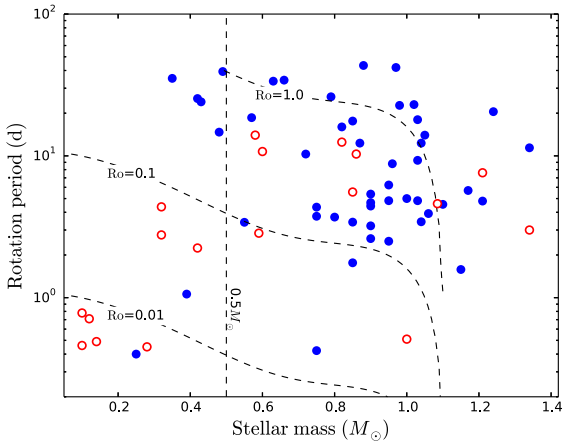

Figure 1. The sample used in this work plotted in rotation-period–mass parameter space. Stars with multiple ZDI maps are plotted with open red points. Dashed lines indicate a stellar mass of 0.5 $M_\odot$ and Rossby numbers of 1.0, 0.1 and 0.01. This is an updated version of fig. 1 from See et al. (2015b).

and decays as r^{-2} on any given field line. The open flux of the star can then be determined by integrating the absolute radial field strength over the source surface as follows:

$$\Phi_{\rm open} = \oint_{r_{\rm ss}} |B_r(r_{\rm ss})| \, {\rm d}S. \tag{4}$$

2.2 Wind speed, density and mass-loss rate

In this work, we will use a similar wind model to that of See et al. (2015a). For the Sun, the wind speed is known to be correlated with the amount of field line divergence of the magnetic field lines (Levine, Altschuler & Harvey 1977; Wang & Sheeley 1990, 1991). Arge & Pizzo (2000) quantified this relationship as

$$v_{\rm wind}\,(r_{\rm Earth}) = 267.5 + \frac{410}{f_{\rm s}^{2/5}} [{\rm km\ s^{-1}}], \tag{5}$$

where the magnetic expansion factor is

$$f_{\rm s} = \left(\frac{r_\star}{r_{\rm ss}}\right)^2 \frac{B(r_\star)}{B(r_{\rm ss})}. \tag{6}$$

In equation (6), $B(r_{\rm ss})$ is the magnetic field strength at a given location on the source surface and $B(r_\star)$ is the magnetic field strength at the stellar surface along the same field line. These values are determined from the field extrapolation using equations (1)–(3). Since we are studying stellar systems, we will assume that equation (5) gives the wind velocity at a distance of $215r_\star$ – the distance at which Earth orbits the Sun.

Similar to See et al. (2015a) and Jardine & Collier Cameron (2008), we use a scaled solar wind density in our model. The wind density is set to be $\rho(r = 215r_\star) = f_{\rm mag} \times 1.7 \times 10^{-23}\,{\rm g\,cm^{-3}}$ at a distance of $215r_\star$, where $f_{\rm mag}$ is the average foot point strength of open field lines normalized to the average solar field strength (1 G) and $1.7 \times 10^{-23}\,{\rm g\,cm^{-3}}$ is the solar wind density at Earth. The scaling, $f_{\rm mag}$, accounts for the denser winds of more active stars (Mestel & Spruit 1987). For the stars in our sample, $f_{\rm mag}$ ranges from $\sim$1 for the least-active solar-like stars to $\sim 3 \times 10^3$ for the most-active M dwarfs.

With knowledge of the wind speed and density, the total mass-loss rate of a star can be calculated by integrating the mass-loss rate per unit surface area over a closed surface encompassing the star beyond the source surface. Due to the way the wind speed and density are calculated, it is convenient to integrate over a spherical surface with a radius of $215r_\star$, i.e.

$$\dot{M} = \oint_{215r_\star} \rho v_{\rm wind} \, {\rm d}S. \tag{7}$$

For an arbitrary stellar wind configuration, the component of the wind normal to the shell would be required to calculate the mass-loss correctly. However, since the wind flows along field lines that are radial past the source surface, the wind vector is, by definition, normal to the integrating surface in our model.

2.3 Angular-momentum-loss rates

In this work, we will make use of the formulations of Matt et al. (2012b, henceforth M12) and Réville et al. (2015a, henceforth R15) in order to estimate angular-momentum-loss rates for our stellar sample. These authors conducted a series of multidimensional MHD simulations exploring the dependence of the angular-momentum-loss rate on various parameters of the star. From these simulations, M12 found the following expression for the angular-momentum-loss rate:

$$\dot{J}_{\rm M12} = K_1^2 B_\star^{4m_1} \dot{M}^{1-2m_1} r_\star^{4m_1+2} \frac{\Omega_\star}{\left(K_2^2 v_{\rm esc}^2 + \Omega_\star^2 r_\star^2\right)^{m_1}}. \tag{8}$$

Building on the work of M12, R15 found the following expression for the angular-momentum-loss rate:

$$\dot{J}_{\rm R15} = \dot{M}\Omega_\star r_\star^2 K_3^2 \left(\frac{\Upsilon_{\rm open}}{\left(1 + f^2/K_4^2\right)^{1/2}}\right)^{2m_2}. \tag{9}$$

In these formulations, $B_\star$ is the equatorial dipolar field strength at the stellar surface, $\dot{M}$ is the mass-loss rate, $r_\star$ is the stellar radius, $\Omega_\star$ is the angular rotation speed, $v_{\rm esc} = (2GM_\star/r_\star)^{1/2}$ is the stellar escape velocity, $f = \Omega_\star r_\star^{3/2}(GM_\star)^{-1/2}$ is the angular rotation speed normalized to the break-up speed, $\Upsilon_{\rm open} = \Phi_{\rm open}^2/(r_\star^2 \dot{M} v_{\rm esc})$ is a measure of the magnetization of the open field lines and $K_1 = 1.3$, $K_2 = 0.0506$, $K_3 = 0.65$, $K_4 = 0.06$, $m_1 = 0.2177$ and $m_2 = 0.31$ are fit parameters determined from the results of simulations.[2] A key assumption of the M12 formulation is a dipolar magnetic field geometry while the R15 formulation encapsulates the effects of more complex field geometries. We shall explore the difference between these two formulations in Section 3.3.

3 RESULTS

3.1 Coronal magnetic field

In Fig. 2, we plot the open flux against rotation period and Rossby number, colour coded by stellar mass. The open flux values are listed in Table 1. The open flux displays a similar behaviour in both figures, increasing with decreasing rotation period/Rossby number and showing a large spread at the lowest rotation periods/Rossby numbers. However, the scatter is reduced when plotting against the Rossby number. A similar reduction in the scatter of other magnetic activity proxies is seen when they are plotted against Rossby number rather than rotation period, most notably X-ray emission (Noyes et al. 1984; Pizzolato et al. 2003; Wright et al. 2011). On the other

[2] The value of K_3 is given as 1.4 by R15. However, this is a typographical error and the true value is $K_3 = 0.65$ (Réville, private communication).

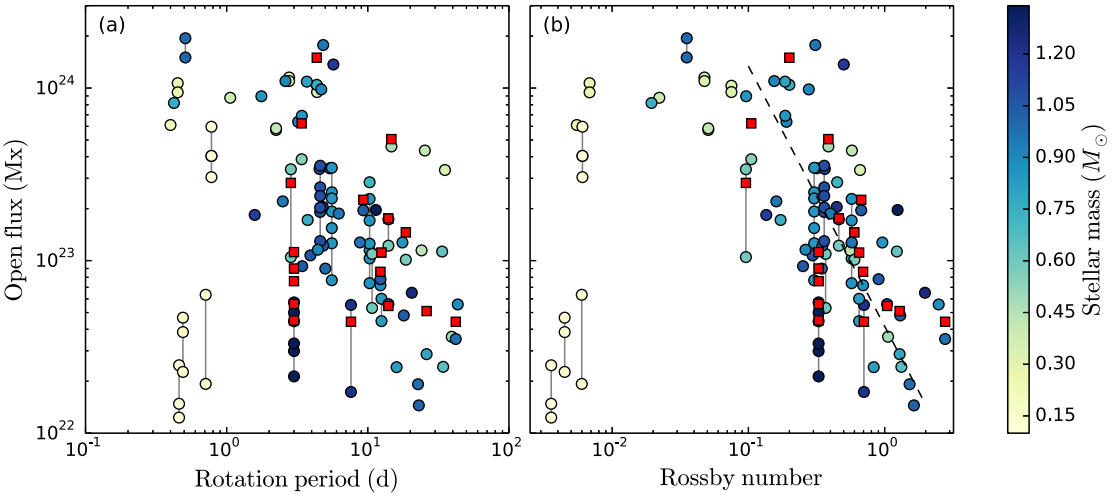

Figure 2. Open flux as a function of (a) rotation period and (b) Rossby number are plotted with circle points. Stars mapped over multiple epochs are joined by a line. Each point is colour coded by stellar mass. Open fluxes calculated from self-consistent 3D MHD simulations are also shown (red squares). The fit to the Ro $>$ 0.1 stars in panel (b) – dashed line – has the form $\Phi_{\rm open}[{\rm Mx}] = (4.16 \pm 0.26) \times 10^{22}\,{\rm Ro}^{-1.51\,\pm\,0.13}$. Data points from 3D MHD simulations (red squares) are not included in the fit.

hand, it should be noted that Reiners, Schüssler & Passegger (2014) argue that the rotation period is a more fundamental parameter than Rossby number in the context of dynamo action.

While Fig. 2(b) looks similar to the classical activity–rotation relationship observed in X-ray studies, there are some noticeable differences. Usually, there is a clear change in behaviour at Ro $\sim$ 0.1 as stars transition from the saturated to unsaturated regimes. The unsaturated regime is still evident in Fig. 2(b) but the saturated regime is less obvious compared to other activity proxies due to the relative dearth of stars with 0.01 $<$ Ro $<$ 0.1 in our sample. At Ro $<$ 0.01, a sharp change in behaviour is observed. In this regime, the open flux values show no dependence on Rossby number and are spread over two orders of magnitude. These are the lowest mass stars in our sample ($<$0.3 $M_\odot$). As discussed previously in the literature, low-mass M dwarfs show two distinct sets of properties: either strong dominantly dipolar fields or weak multipolar fields (Morin et al. 2010). This explains why there is such a large spread of open flux values in such a narrow Rossby number range. Given the uncertainty in the behaviour in the Ro $<$ 0.1 regime, we perform a fit to the stars with Ro $>$ 0.1 only. This fit has the form

$$\Phi_{\rm open}[{\rm Mx}] = (4.16 \pm 0.26) \times 10^{22}\,{\rm Ro}^{-1.51\pm0.13} \quad (10)$$

and is shown as a dashed line in Fig 2(b). All the fits in this paper used the bisector ordinary least-squares method (Isobe et al. 1990). The errors in the fit are calculated only by considering the scatter in the points without considering the intrinsic error in the individual data points. It is important to note that the form of this fit, as well as other fits presented in the rest of this work, will depend on the adopted convective turnover times. We have chosen to use the empirically determined prescription of Wright et al. (2011) but different prescriptions may produce slightly different fits. Vidotto et al. (2014b) determined fits for the surface flux and unsigned average magnetic field strength as a function of Rossby number for a sample of stars similar to the one used in this work. These authors tested a number of different prescriptions for the convective turnover time and found that, while the fit values changed, they did agree to within 2σ (see their appendix A5).

A number of the stars in our sample have also been modelled using self-consistent 3D MHD simulations that incorporate the same ZDI maps that we use in this work (see Section 3.4 for further discussion). We have plotted the open flux values of these stars, from the MHD simulations, using red squares in Fig. 2. It is clear that the MHD values all fall within the general trend shown by the PFSS model values.

It is worth considering how the resolution of the ZDI maps may affect the results of these extrapolations. The highest spherical harmonic mode that can be reconstructed by ZDI depends on the $v \sin i$ of the star in question (see Morin et al. 2010 and Fares et al. 2012 for further details). Within our sample, most maps have $l_{\rm max}$ values between 5 and 10. Jardine, Vidotto & See (2017) conducted a systematic study of the dependence of a PFSS extrapolation on the resolution of the magnetic map used. These authors took magnetograms of the Sun over two solar cycles and calculated the total magnetic flux at the stellar surface and the open flux. They repeated this process, truncating the $l_{\rm max}$ of the maps to lower values and found that the surface flux increased with higher $l_{\rm max}$ but that the open flux had very little dependence on $l_{\rm max}$. Indeed, the amount of open flux is determined predominantly by the dipole component of the Sun's magnetic field. This is not surprising given that the dipole component decays most slowly with increasing height from the stellar surface. In Fig. 3(a), we plot the average unsigned magnetic field strength in the dipole component of the ZDI map, $\langle|B_{\rm dip}|\rangle$, against the open flux for our sample of stars. The symbol colours and meanings are the same as Fig. 2. Broadly, the trend is of increasing open flux with increasing dipole field strength. However, there is a large amount of scatter in the plot. This can be attributed to the different radii of the stars in our sample. Indeed, the influence of the stellar mass, and hence radii, can be seen in Fig. 3(a) where the colours of the points vary systematically across the plot. In Fig. 3(b), we account for this effect by plotting the dipole field strength against the open flux normalized by the stellar surface area.[3] All the points collapse on to a very narrow relation given by $\langle|B_{\rm dip}|\rangle = (2.97 \pm 0.02)(\Phi_{\rm open}/4\pi r_\star^2)^{(1.011\pm0.003)}$. The fact

[3] The units of $\Phi_{\rm open}/4\pi r_\star^2$ are Mx cm^{-2}. Dimensionally, this is equivalent to a magnetic field strength measured in Gauss. However, the quantity $\Phi_{\rm open}/4\pi r_\star^2$ does not correspond to any physically meaningful field strength and so we opt to express it in this form. Additionally, this form will be more useful for future studies since the open flux of a star can be easily estimated from the dipole field strength and stellar radii.

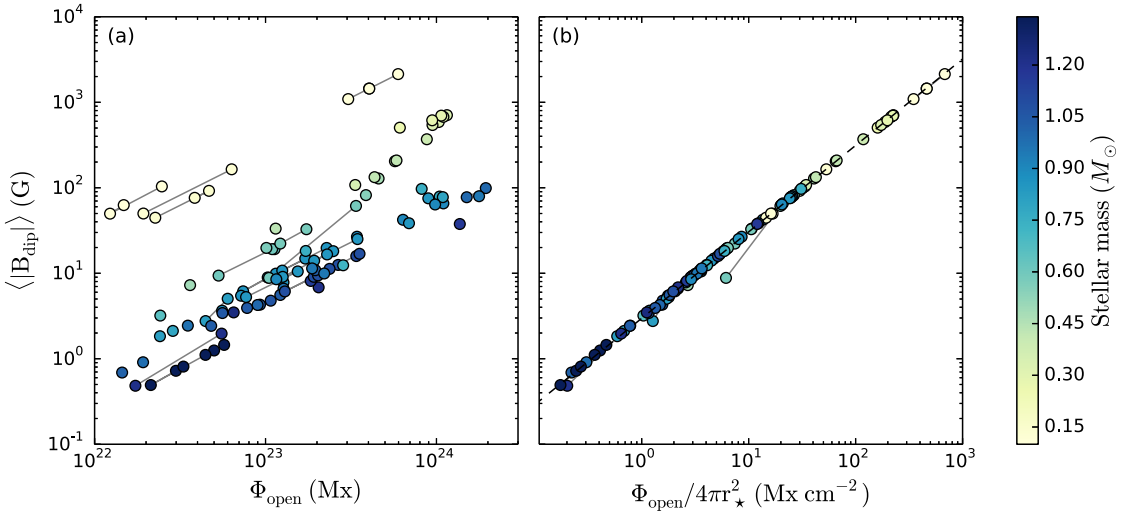

Figure 3. Average unsigned magnetic field strength of the dipole component ($l = 1$) at the stellar surface against (a) the open flux and (b) the open flux normalized by stellar surface area. Symbol colours and meanings are the same as Fig. 2. The dashed line in panel (b) is a power-law fit of the form $\langle|B_{dip}|\rangle = (2.97 \pm 0.02)(\Phi_{open}/4\pi r_\star^2)^{(1.011\pm0.003)}$.

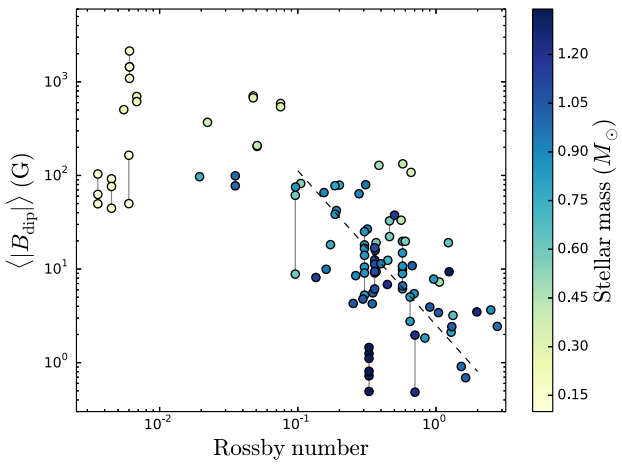

Figure 4. Average unsigned magnetic field strength of the dipole component ($l = 1$) at the stellar surface against Rossby number. Symbol colours and meanings are the same as Fig. 2. The fit to the Ro > 0.1 stars has the form $\langle|B_{dip}|\rangle = (2.52 \pm 0.20)\,\mathrm{Ro}^{-1.65\pm0.14}$.

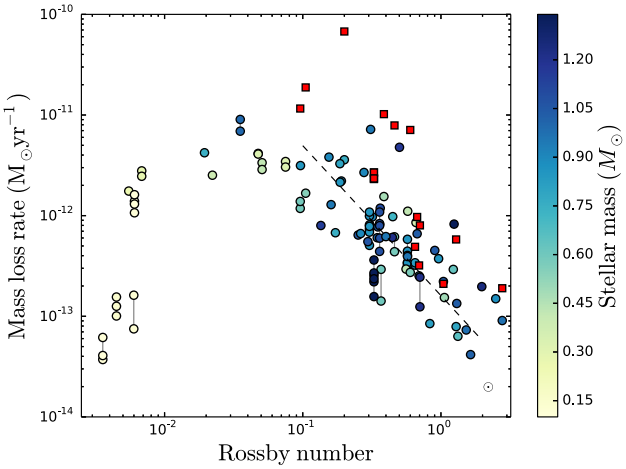

Figure 5. Predicted mass-loss rate against Rossby number. Symbol colours and meanings are the same as Fig. 2. The fit to the Ro > 0.1 stars (dashed line) has the form $\dot{M}[\mathrm{M}_\odot\,\mathrm{yr}^{-1}] = (1.60 \pm 0.09) \times 10^{-13}\ \mathrm{Ro}^{-1.49\pm0.13}$. Data points from 3D MHD simulations (red squares) are not included in the fit.

that all the points lay on such a tight sequence and the power index of $\sim$1 demonstrates that it is predominantly the dipole components of the magnetic field that determines the open flux of a star, at least for this choice of source surface radii. It should be expected that for sufficiently small choices of the source surface radii, higher order field modes will affect the value of the open flux (see Section 3.3.2 for further discussion of the impact of the source surface radius). For completeness, we plot $\langle|B_{dip}|\rangle$ against Rossby number in Fig. 4. The fit to the Ro > 0.1 stars (dashed line) has the form $\langle|B_{dip}|\rangle = (2.52 \pm 0.20)\,\mathrm{Ro}^{-1.65\pm0.14}$. Together, Figs 2(b), 3(a) and 4 show the three possible 2D projections of our sample in ($\langle|B_{dip}|\rangle$, Φ_{open}, Ro) space.

3.2 Mass-loss rates

In Fig. 5, we plot the mass-loss rate, as estimated using the method described in Section 2, against Rossby number for our sample of stars. The mass-loss rates for each star are listed in Table 1. As with the open flux, the scatter in the plot is reduced when plotting against Rossby number rather than rotation period (not shown). The fit to the Ro > 0.1 stars (dashed line) has the form

$$\dot{M}[\mathrm{M}_\odot\,\mathrm{yr}^{-1}] = (1.60 \pm 0.09) \times 10^{-13}\ \mathrm{Ro}^{-1.49\pm0.13}. \quad (11)$$

The overall shape of this plot is very similar to that of Fig. 2(b) (Φ_{open} versus Ro). This is to be expected given the model we have used to estimate the mass-loss rates. The presence of the scaling factor, f_{mag}, that accounts for the stronger winds of more active stars, means that the wind density will scale with the surface magnetic field strength. However, the mass-loss rate also has a dependence on the surface area of the star, just as the open flux does, explaining why our predicted mass-loss rates and open fluxes have the same qualitative dependence on Rossby number. Our predicted mass-loss rates are in good agreement with the estimates derived from self-consistent MHD simulations (red squares) at larger Rossby numbers. However, the MHD estimates appear to have a steeper dependence on Rossby

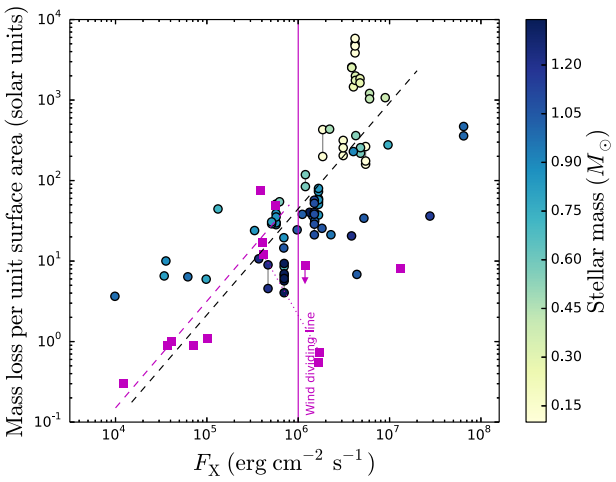

Figure 6. Mass-loss rate per unit surface area against surface X-ray flux. Symbol colours and meanings are the same as Fig. 2. The black dashed line is a power-law fit to the whole sample of the form $\frac{\dot{M}/r_\star^2}{\dot{M}_\odot/r_\odot^2} = (5.51 \pm 4.89) \times 10^{-7}\ F_X^{1.32\pm0.15}$. Fitting to the $M_\star > 0.5\,M_\odot$ stars only, we find a fit of $\frac{\dot{M}/r_\star^2}{\dot{M}_\odot/r_\odot^2} = (5.01 \pm 2.53) \times 10^{-4}\ F_X^{0.79\pm0.08}$ (fit line not shown). Overplotted in magenta are the indirect mass-loss rate estimates of Wood et al. (2014, square symbols), their wind dividing line (solid line) and their fit to their stars below the wind dividing line given by, $\dot{M}/r_\star^2 \propto F_X^{1.34}$ (dashed line).

number and differ by an order of magnitude or more at smaller Rossby numbers. This is not necessarily surprising given that both models are calibrated using solar values. One way to improve the agreement of the $\dot{M}$ estimates would be to adjust the wind density in the PFSS or MHD model (or both). The wind density is controlled by the $f_{\rm mag}$ parameter in our PFSS model and by the base density of the wind, n_0, in the MHD models. Fig. 5 suggests that the ratio of these two model parameters, $n_0/f_{\rm mag}$, is larger for stars with lower Rossby numbers. Better agreement would likely be found if the models were formulated such that $n_0/f_{\rm mag}$ remained constant as a function of Rossby number.

Currently, the best observational constraints on the mass-loss rates of low-mass stars come from indirect estimates based on Lyα observations (Wood 2004). This author has estimated the mass-loss rates of ∼10 stars and found that they have a power-law dependence on the surface X-ray flux of $\dot{M}/r_\star^2 \propto F_X^{1.34}$ (Wood et al. 2005). However, this trend appears to break down for the most active stars. A number of stars with $F_X > 10^6$ erg cm^{-2} s^{-1} seem to have substantially lower mass-loss rates than expected from the stated power law (Wood et al. 2014). These authors suggest that some mechanism, such as a change in magnetic field geometry, inhibits the mass-loss rates of the most active stars and call this divide the 'wind dividing line'. In Fig. 6, we reproduce the mass-loss rate versus F_X plot of Wood et al. (2014, their fig. 4) with magenta squares as well as their wind dividing line. Additionally, we also plot our mass-loss estimates. A power-law fit to our sample with the form $\frac{\dot{M}/r_\star^2}{\dot{M}_\odot/r_\odot^2} = (5.51 \pm 4.89) \times 10^{-7}\ F_X^{1.32\pm0.15}$ is shown by the black dashed line. Overall, our mass-loss rates increase with activity, albeit with some scatter. Below the wind dividing line, our mass-loss rates increase with increasing activity, which is in qualitative agreement with the results of Wood et al. (2014). While our mass-loss rates appear to be larger than theirs at the lowest activities, the power-law index of our fit, 1.32, is remarkably close to their value of 1.34. However, this may be a coincidence. By eye, the mass-loss rates of the stars in our sample below the wind dividing line clearly having a shallower dependence on F_X than the Lyα sample. Additionally, the fit is influenced by the presence of stars with $M_\star < 0.5\,M_\odot$. These stars are known to have different magnetic field properties, most likely as a result of different internal structures to their higher mass counter parts (Donati et al. 2008; Morin et al. 2008b). Removing these stars, we obtain a fit of $\frac{\dot{M}/r_\star^2}{\dot{M}_\odot/r_\odot^2} = (5.01 \pm 2.53) \times 10^{-4}\ F_X^{0.79\pm0.08}$.

Unlike Wood et al. (2014), our estimated mass-loss rates continue to increase with increasing activity beyond the wind dividing line. Indeed, we see no substantial change in behaviour in our sample across the $F_X = 10^6$ erg cm^{-2} s^{-1} line. This result is in agreement with previous mass-loss simulations that have also found no change in behaviour over the wind dividing line (See et al. 2014; Johnstone et al. 2015) as well as the study of Vidotto et al. (2016). This latter study looked at the large-scale magnetic topologies of all the stars studied by Wood et al. (2014) that had ZDI maps and found that there was no abrupt change in their magnetic field properties over the wind dividing line. Given the small number of stars in the study of Wood et al. (2014), it remains to be seen whether the idea of a wind dividing line will survive after more stars have had their mass-loss rates estimated with the Lyα technique. On the other hand, if it emerges that stars with $F_X > 10^6$ erg cm^{-2} s^{-1} truly do suffer from reduced mass-loss rates, it would be an indication that current models of mass-loss are missing important physics.

3.3 Angular-momentum loss

3.3.1 Trends with Rossby number

In Fig. 7(a), we show the angular-momentum-loss rate, as calculated with the R15 braking law (equation 9), against Rossby number. The angular-momentum-loss rate shows a similar qualitative behaviour to the open flux (Fig. 2b) and mass-loss rate (Fig. 5); increasing $\dot{J}_{\rm R15}$ with decreasing Rossby number and a large spread in $\dot{J}_{\rm R15}$ below Ro ∼ 0.01. This is unsurprising given the dependence of the angular-momentum-loss rate on the open flux and mass-loss rate. The fit to the Ro > 0.1 stars (dashed line) has the form

$$\dot{J}_{\rm R15}[{\rm erg}] = (4.65 \pm 0.47) \times 10^{30}\ {\rm Ro}^{-3.19\pm0.25}. \quad (12)$$

In Fig. 7(b), we show the instantaneous spin-down time-scale, $\tau_{\rm R15} = J/\dot{J}_{\rm R15}$ for our sample of stars. Values for both $\dot{J}_{\rm R15}$ and $\tau_{\rm R15}$ are listed in Table 1. In order to calculate the angular momentum, $J = I\Omega_\star$, we require the moments of inertia, I, for each star. These were estimated using the evolutionary models of Baraffe et al. (2015) at an age of 500 Myr. This should be representative of the moments of inertia for these stars since they do not evolve significantly over their main-sequence lifetime. The fit to the Ro > 0.1 stars (dashed line) has the form $\tau_{\rm R15} = (20.0 \pm 1.9)\,{\rm Ro}^{2.34\pm0.22}$. The angular-momentum-loss rates and spin-down time-scales[4] estimated from MHD simulations (red squares) agree well with our results. This is in spite of the fact that the PFSS and MHD estimates for the mass-loss rates used to calculate the angular-momentum-loss rate show larger disagreements (Section 3.2). The reason for this is that the angular-momentum-loss rate (equation 9) has a much

[4] Our method of estimating the stellar angular momentum, J, differs from the method used by the MHD simulations. Therefore, we have recalculated the spin-down time-scales for the MHD simulations using our angular-momentum values to provide a consistent comparison to our model results.

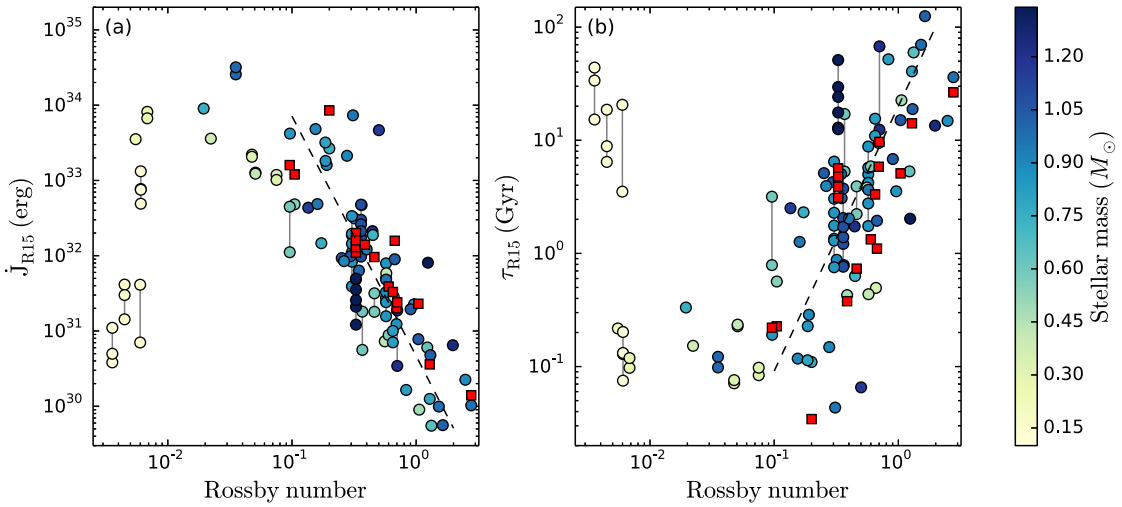

Figure 7. (a) Angular-momentum-loss rates, $\dot{J}_{R15}$ and (b) spin-down time-scale, τ_{R15}, against Rossby number. Symbol colours and meanings are the same as Fig. 2. The fits to the Ro > 0.1 stars have the form $\dot{J}_{R15}[\mathrm{erg}] = (4.65 \pm 0.47) \times 10^{30}\ \mathrm{Ro}^{-3.19\pm0.25}$ in panel (a) and $\tau_{R15}[\mathrm{Gyr}] = (20.0 \pm 1.9)\,\mathrm{Ro}^{2.34\pm0.22}$ in panel (b). Data points from 3D MHD simulations (red squares) are not included in the fit.

stronger dependence on the open flux, $\dot{J}_{R15} \propto \Phi_{\mathrm{open}}^{4m_2} \propto \Phi_{\mathrm{open}}^{1.24}$, compared to the mass-loss rate, $\dot{J}_{R15} \propto \dot{M}^{1-2m_2} \propto \dot{M}^{0.38}$.

The angular-momentum-loss rates of stars with Ro > 0.01 decrease as a function of Rossby number. Correspondingly, the spin-down time-scale increases with Rossby number. This is a simple consequence of stellar activity declining as stars spin-down over their lifetimes. However, the spin-down behaviour of stars with Ro < 0.01 is much more intriguing. This regime consists of all the $M_\star < 0.2\,\mathrm{M}_\odot$ stars whose magnetic fields exist in one of two distinct states (Morin et al. 2010), as well as a number of slightly higher mass stars (all $<0.28\,\mathrm{M}_\odot$). The two distinct set of magnetic characteristics has resulted in two groups of stars. Those with strong dipolar fields (V374 Peg, EQ Peg B and WX UMa) have large angular-momentum-loss rates and lie roughly at the tail end of the sequence of Ro > 0.01 stars with spin-down time-scales of $\tau_{R15} \sim 100$–200 Myr. However, the stars with weak and more complex field structures (DX Cnc, GJ 1156 and GJ 1245B) have angular-momentum-loss rates that are two orders of magnitude weaker compared to their strong-field counterparts, despite having comparable Rossby numbers. These stars have much longer spin-down scales of the order of $\tau_{R15} \sim 3$–40 Gyr. It is perhaps odd that the stars in both the strong- and weak-field states have similar rotation periods despite the large difference in the spin-down time-scales. A coherent theory of angular-momentum evolution of these types of stars will need to explain how this is possible.

3.3.2 *Comparing braking laws*

At this stage, it will be instructive to compare the M12 and R15 braking laws and their ability to predict the angular-momentum-loss rate of a star. The R15 braking law is formulated to account for the effects of complex magnetic field geometries whereas the M12 braking law was constructed by considering only dipolar geometries. However, the R15 braking law is expressed in terms of the open flux while the M12 braking law is expressed in terms of the surface field strength of the dipolar component. While better capturing the effects of complex field geometries, this means that the R15 law is also, in practice, more difficult to use since the open flux of a star is a more difficult quantity to obtain or estimate. In particular, when using the PFSS model, accurately estimating the open flux of a star will require an accurate estimate of the source surface radius, which is a free parameter of the model.

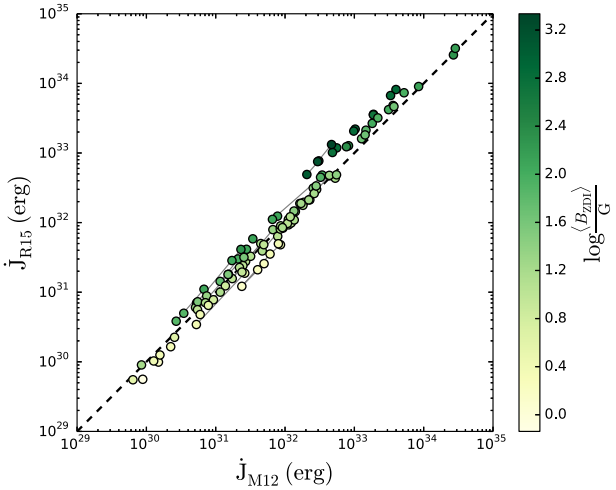

Figure 8. Comparison of angular-momentum-loss rates as estimated by the braking laws of M12 and R15. The dashed line indicates $\dot{J}_{R15} = \dot{J}_{M12}$. Each point is colour coded by the average magnetic field strength at the stellar surface.

In Section 3.1, we showed that the open flux is dominated by the dipole component of the field, which suggests that the M12 braking law is sufficient to provide an accurate estimate of the angular-momentum-loss rate of a star. In Fig. 8, we compare the angular-momentum-loss rates as calculated by the formulations of M12 and R15, the values of which are listed in Table 1. When calculating $\dot{J}_{R15}$ and $\dot{J}_{M12}$, the open flux, as shown in Fig. 2, and the average surface field strengths of the dipolar component, as shown in Fig. 3, are used, respectively. The two formulations agree very well with most stars agreeing to within a factor of ∼1.5. Even the stars with the largest discrepancies still agree to within a factor of ∼3.

When interpreting Fig. 8, there are a number of factors of which we must be mindful. First, our result that the open flux is predominantly determined by the dipolar component of the field is based

on the assumed source surface radii of $r_{ss} = 3.41r_{\star}$ for all our stars. However, the source surface radius is a free parameter within our model. If the source surface radius is actually smaller than our chosen value, higher order multipoles may have a non-negligible effect on the open flux making the M12 formulation less accurate. Secondly, the R15 formulation is also dependent on our choice of source surface radius. For a given input ZDI map, the open flux decreases for larger choices of the source surface radius and vice versa. In reality, one would expect the source surface radius to vary as a function of the fundamental parameters of a star (Réville et al. 2015b).

It is interesting to note that there is a systematic trend with the average surface magnetic field strength, $\langle B_{ZDI} \rangle$, in Fig. 8. The $\dot{J}_{R15} > \dot{J}_{M12}$ stars have the strongest surface magnetic fields, and, conversely, $\dot{J}_{R15} < \dot{J}_{M12}$ stars have the weakest. It is not unreasonable to suggest that stars with stronger magnetic fields may have larger source surface radii. Increasing the source surface radii of the $\dot{J}_{R15} > \dot{J}_{M12}$ (strong field) stars would reduce their open flux and bring their $\dot{J}_{R15}$ estimates closer to their $\dot{J}_{M12}$ estimates. Conversely, reducing the source surface radii of the $\dot{J}_{R15} < \dot{J}_{M12}$ (weak field) stars would increase their open flux and also bring their $\dot{J}_{R15}$ estimates closer to their $\dot{J}_{M12}$ estimates. Of course, we should remember that our aim is not necessarily to make the $\dot{J}_{R15}$ estimates match the $\dot{J}_{M12}$ estimates since, as we have already discussed, the $\dot{J}_{M12}$ formulation will become less accurate for stars where higher order field mores are not negligible.

It is clear that the source surface radius is an important parameter to set properly. Fig. 8 shows that the M12 and R15 formulations are in reasonable agreement. It is likely that both of these formulations, as implemented in this work, can provide a reasonably reliable estimate of the angular-momentum-loss rate of a star. This is especially true when considering that the discrepancies between the M12 and R15 formulations are much smaller than the scatter in the physical properties input into these formulations, e.g. open flux. However, the issues of higher order field modes and our assumption of a constant source surface radius means that neither formulation, as implemented in this work, are perfect estimates. Further investigation will be required to determine when the M12 formulation is valid to use (since it is the easier formulation to use) and what source surface radius to use when the R15 formulation is used.

3.4 Comparison to 3D MHD simulations

MHD simulations have an advantage over the model used in this work because they include more self-consistent physics at the cost of being much more computationally expensive. A computationally cheaper model, such as the one we have presented here, is therefore required to model this many stars within a reasonable time frame. Both types of model suffer from the fact that wind densities are difficult to constrain observationally. With these points in mind, it is important to study the differences in the models in order to understand how the choice of model affects the end results.

The MHD simulations that we compare to, make use of the BATS-R-US numerical code (Powell et al. 1999). This is a 3D code that solves the ideal MHD equations on an adaptive mesh grid in Cartesian coordinates. The simulations require an initial magnetic field and stellar wind configuration. The wind is initialized using a thermally driven Parker wind (Parker 1958) while the 3D magnetic field structure is initialized using a ZDI map and the PFSS model. The wind and field are then allowed to interact self-consistently until the simulation relaxes to a steady-state solution. As discussed in Section 3.2, the base wind density is a free parameter within these simulations.

We have demonstrated that our results broadly agree with those of the MHD simulations. It is clear that the open flux (Fig. 2), angular-momentum-loss rates (Fig. 7a) and instantaneous spin-down time-scales (Fig. 7b) calculated from MHD simulations lie within the scatter of the results from our own models. While the mass-loss estimates agree reasonably well for low-activity stars, the agreement becomes worse at lower Rossby numbers (Fig. 5). This is likely due to the different choices of wind densities in the models (see Section 3.2). On the whole, our model appears to produce reasonable values and trends for these parameters.

As well as comparing overall trends, we can make a direct comparison of the models for each of the stars that have been modelled with an MHD code. In Table 2, we list estimates for the open flux, mass-loss rate, angular-momentum-loss rate and instantaneous spin-down time-scale from both models, as well as the ratio of the values obtained under both models. The open fluxes show a very good agreement – within a factor of $\sim$2 for the large majority of the stars. The mass-loss rates on the other hand match less well. In some cases, the mass-loss rates obtained from our PFSS model and the MHD models differ by an order of magnitude or more. In particular, the discrepancy is larger for M dwarf stars. As discussed in Section 3.2, a better agreement between the models could be found by adjusting the wind densities in each of the models. The angular-momentum-loss rates, $\dot{J}$, and spin-down time-scales, τ, both show a reasonable agreement. These values agree to within a factor of $\sim$4 for the majority of the stars. As with the mass-loss rates, the angular-momentum-loss rates estimated from our PFSS model are lower than the values obtained from the MHD models. Given the dependence of $\dot{J}$ on $\dot{M}$ (see equation 9), reducing the discrepancy in $\dot{M}$ between the models would also decrease the discrepancy in $\dot{J}$. Overall, our computationally efficient PFSS model provides a reasonable match to the MHD models although there is still room for improvement.

4 DISCUSSION AND CONCLUSIONS

In recent years, large strides have been made in understanding the factors that affect the rotational evolution of main-sequence stars. In particular, the dependence of the angular-momentum-loss rate on the open flux of a star has been quantified through the use of MHD simulations (Vidotto et al. 2014a; R15). Formulating a braking law in terms of the open flux is an improvement over previous implementations since it accounts for the complex magnetic field geometries that stars are known to have. In principle, such a braking law can be used to compute the rotation-period evolution of a star over its main-sequence lifetime. However, there have been little to no systematic studies investigating how the open flux varies as a function of fundamental stellar parameters.

In this work, we use a sample of stars that have had their large-scale surface magnetic fields mapped using the ZDI technique to study various parameters related to stellar spin-down. This is the largest sample of ZDI maps assembled in one study to date. Using the PFSS method, we analyse how the open flux of these stars, as well as their mass-loss rates, angular-momentum-loss rates and instantaneous spin-down time-scales vary as a function of fundamental stellar parameters. The choice to use a PFSS model was driven by the requirement of a computationally efficient method with which to model our large sample. Indeed, attempting to model all our stars with a multidimensional MHD model would have taken a prohibitively long amount of time. Our results indicate that the PFSS model provides results that are in reasonable agreement with MHD models.

MNRAS 466, 1542–1554 (2017)

Table 2. Comparison of the results from the our model (denoted as 'PFSS') with the results from 3D MHD models (denoted as 'MHD'). For each star, we list the open flux, $\Phi_{\rm open}$, mass-loss rate, $\dot{M}$, angular-momentum-loss rate, $\dot{J}$, and instantaneous spin-down time-scale, τ, from our model and the MHD models. Additionally, we list the ratio of each of these quantities from the two models given by dividing the MHD model value by the PFSS model value. References indicate the original article in which the MHD models were published. It should be noted that the MHD spin-down time-scales, $\tau_{\rm MHD}$, have been recalculated and are not the same as the values published in the original articles (see discussion in Section 3.4).

Star ID	$\Phi_{\rm open}^{\rm PFSS}$ (10^{22} Mx)	$\Phi_{\rm open}^{\rm MHD}$ (10^{22} Mx)	Ratio ($\Phi_{\rm open}$)	$\dot{M}_{\rm PFSS}$ ($10^{-12}\,{\rm M}_\odot\,{\rm yr}^{-1}$)	$\dot{M}_{\rm MHD}$ ($10^{-12}\,{\rm M}_\odot\,{\rm yr}^{-1}$)	Ratio ($\dot{M}$)	$\dot{J}_{\rm R15}^{\rm PFSS}$ (10^{32} erg)	$\dot{J}^{\rm MHD}$ (10^{32} erg)	Ratio ($\dot{J}$)	$\tau_{\rm R15}^{\rm PFSS}$ (Gyr)	$\tau^{\rm MHD}$ (Gyr)	Ratio (τ)	Ref.
HD 189733 (2008 July)	6.01	11.14	1.85	0.32	0.49	1.53	0.1	0.33	3.30	10.94	3.32	0.30	1
GJ 49	10.1	14.56	1.44	0.27	7.1	26.30	0.088	0.39	4.43	5.88	1.33	0.23	2
CE Boo	45.9	50.6	1.10	1.55	10.2	6.58	1.24	1.4	1.13	0.43	0.38	0.89	2
DS Leo (2007 Dec)	12.2	17.55	1.44	0.44	7.88	17.91	0.18	0.96	5.33	3.92	0.73	0.19	2
GJ 182	104	150	1.44	3.59	67.6	18.83	26.6	85	3.20	0.11	0.034	0.31	2
OT Ser	38.7	62.4	1.61	1.67	18.8	11.26	4.8	12	2.50	0.56	0.23	0.41	2
DT Vir (2007 Jan)	33.8	28.2	0.83	1.18	11.6	9.83	4.48	16	3.57	0.79	0.22	0.28	2
HD 46375	3.51	4.42	1.26	0.09	0.19	2.11	0.01	0.014	1.40	36.11	26.5	0.73	3
HD 73256	5.59	5.46	0.98	0.22	0.21	0.95	0.078	0.23	2.95	15.06	5.09	0.34	3
HD 102195	7.19	8.61	1.20	0.25	0.32	1.28	0.12	0.2	1.67	9.47	5.84	0.62	3
HD 130322	2.87	5.11	1.78	0.08	0.58	7.25	0.013	0.036	2.77	40.62	14.1	0.35	3
HD 179949 (2007 June)	1.73	4.42	2.55	0.12	0.8	6.67	0.034	0.24	7.06	67.66	9.68	0.14	3
HD 20630	19.56	22.5	1.15	0.66	0.97	1.47	0.9	1.58	1.76	1.94	1.1	0.57	4
τ Boo (2009 May)	4.45	4.5	1.01	0.24	2.34	9.75	0.35	1.3	3.71	17.60	4.78	0.27	5
τ Boo (2010 Jan)	5	7.6	1.52	0.36	2.31	6.42	0.48	2	4.17	12.94	3.11	0.24	5
τ Boo (2011 Jan)	5.72	5.6	0.98	0.25	2.34	9.36	0.49	1.6	3.27	12.52	3.89	0.31	5

1: Llama et al. (2013); 2: Vidotto et al. (2014a); 3: Vidotto et al. (2015); 4: do Nascimento et al. (2016); 5: Nicholson et al. (2016).

We find that the open flux for the majority of our stars is predominantly determined by the dipole component of the magnetic field for our choice of the source surface radii ($r_{ss} = 3.41 r_\star$). Similarly to previous studies of other proxies of magnetic activity (e.g. Wright et al. 2011), the open flux, mass-loss rates and angular-momentum-loss rates all show less scatter when plotted against Rossby number rather than rotation period. In the unsaturated regime (Ro $\gtrsim 0.1$), each of these parameters increase with decreasing Rossby number. At Ro $\lesssim 0.1$, magnetic proxies typically saturate. We also see evidence of saturation in the open flux, mass-loss rates and angular-momentum-loss rates although it is not as clear as it is for other magnetic proxies because of a dearth of stars in our sample in this regime. When comparing to mass-loss rates estimated from the Lyα technique, we do not predict a drop in mass-loss rates above the wind dividing line as Wood et al. (2014) suggest. Further work will be required to determine the reason for this difference in mass-loss rate behaviour at the highest activities. Clarifying how mass-loss rates evolve over time, especially early on in the lifetime of a star, will be crucial to understanding whether potentially habitable planets can retain their atmospheres (e.g. Ribas et al. 2016).

At the smallest Rossby numbers (Ro $\lesssim 0.01$), the behaviour of the open flux, mass-loss and angular-momentum-loss rates changes abruptly. Due to the presence of both strong dipolar magnetic fields and weak multipolar fields in the lowest mass stars (Morin et al. 2010), the open flux, mass-loss rates, angular-momentum-loss rates and spin-down time-scales of these stars are spread out over many orders of magnitude over a very narrow range of Rossby numbers. Models of angular-momentum evolution (e.g. Reiners & Mohanty 2012; Matt et al. 2015) typically do not account for both the strong- and weak-field states in the lowest mass M dwarfs. The model of Reiners & Mohanty (2012) predicts long spin-down time-scales for the lowest mass stars due to their small stellar radii. Our model also predicts long spin-down time-scales for the low-mass M dwarfs but only for the weak multipolar stars. Unlike the model of Reiners & Mohanty (2012), we simultaneously predict a population of low-mass M dwarfs with much shorter spin-down time-scales, i.e. those with strong dipolar fields.

A number of suggestions have been proposed to explain the two magnetic field states observed for the lowest mass M dwarfs. The first is that a parameter other than rotation and mass, such as age, may have an effect. Indeed, Morin et al. (2010) discuss the possibility these stars switch from a weak multipolar state to a strong dipolar state at some point in their lifetimes. This suggestion is supported by the fact that the weak-field stars in their sample belong to a young kinematic population while the strong-field stars belong to older kinematic populations. Another suggestion is that these stars switch repeatedly between the two states as part of some form of magnetic cycle on the time-scale of decades (Morin et al. 2010; Kitchatinov, Moss & Sokoloff 2014). Finally, it may be the case that these stars occupy a bistable region of parameter space such that two different stable field configurations are possible for a very similar set of stellar parameters (Morin et al. 2011; Gastine et al. 2013). Under this scenario, the dynamos of these stars would be capable of generating either strong or weak surface magnetic fields but would not be expected to switch between them.

The spread in field strengths, and hence angular-momentum-loss rates, at Rossby numbers less than 0.01 has implications for the rotation-period evolution of these stars. Such a large spread in spin-down times may go some way to explaining the spread in rotation periods observed in low-mass M dwarfs (e.g. Irwin et al. 2011; Douglas et al. 2016; Newton et al. 2016). Additionally, each of the scenarios discussed should produce different rotation-period distributions at late ages. For instance, under the bistability scenario, one might expect to observe a population of fast rotators and a population of slow rotators. On the other hand, the effects of a star switching between strong- and weak-field states should average out over evolutionary time-scales, possibly resulting in these stars converging to a narrow range of rotation periods at late ages. Finally, as part of the MEarth project, Newton et al. (2016) measured the rotation periods of several hundred mid M dwarfs and found the distribution to be consistent with a scenario of rapid rotation for several Gyr followed by rapid spin-down. Such a scenario would be compatible with the idea that these stars switch from a weak-field to strong-field state at some point within their lifetimes. It is also curious that a significant fraction of the Ro < 0.01 stars are in the strong dipole field state considering how much shorter their spin-down time-scales are when compared to the weak-field counterparts. The fact that the exact ages of the strong/weak-field stars in our sample are unknown prevent us from conducting a detailed study of them in the context of rotation-period data from clusters of known ages.

While significant progress has been made in the field of rotational-period evolution of main-sequence stars, there still remain open questions. For instance, what is the long-term magnetic evolution of Ro < 0.01 M dwarfs? Further rotation-period measurements of fully convective M dwarfs and further ZDI reconstructions of M dwarfs in this regime will be required to answer this question. In this context, SPIRou, a near-infrared spectropolarimeter in construction for the Canada–France–Hawaii Telescope (CFHT; Moutou et al. 2015, first light expected in 2017), should greatly improve our understanding, especially for fully convective M dwarfs with long rotation periods. Additionally, under what circumstances is the dipole component of the magnetic field enough to accurately determine the open flux of a star? Answering these and other questions will be important in developing a truly holistic understanding of the coherent rotational-period evolution seen in open clusters.

ACKNOWLEDGEMENTS

The authors thank an anonymous referee for the constructive comments that helped improve this work. VS acknowledges the support of a Science and Technology Facilities Council (STFC) postdoctoral fellowship. SBS and SVJ acknowledge research funding by the Deutsche Forchungsgemeinschaft (DFG) under grant SFB, project A16. This study was supported by the grant ANR 2011 Blanc SIMI5-6 020 01 'Toupies: Towards understanding the spin evolution of stars' (http://ipag.osug.fr/Anr_Toupies/). This work is based on observations obtained with ESPaDOnS at the CFHT and with NARVAL at the TBL. CFHT/ESPaDOnS are operated by the National Research Council of Canada, the Institut National des Sciences de l'Univers of the Centre National de la Recherche Scientifique (INSU/CNRS) of France and the University of Hawaii, while TBL/NARVAL are operated by INSU/CNRS. We thank the CFHT and TBL staff for their help during the observations.

REFERENCES

Allain S., 1998, A&A, 333, 629
Altschuler M. D., Newkirk G., 1969, Sol. Phys., 9, 131
Alvarado-Gómez J. D., Hussain G. A. J., Cohen O., Drake J. J., Garraffo C., Grunhut J., Gombosi T. I., 2016, A&A, 588, A28
Amard L., Palacios A., Charbonnel C., Gallet F., Bouvier J., 2016, A&A, 587, A105
Arge C. N., Pizzo V. J., 2000, J. Geophys. Res., 105, 10465
Balikhin M., Gedalin M., Petrukovich A., 1993, Phys. Rev. Lett., 70, 1259

Baraffe I., Homeier D., Allard F., Chabrier G., 2015, A&A, 577, A42
Barnes S. A., 2003, ApJ, 586, 464
Barnes S. A., 2010, ApJ, 722, 222
Barnes S. A., Weingrill J., Fritzewski D., Strassmeier K. G., Platais I., 2016, ApJ, 823, 16
Blackman E. G., Owen J. E., 2016, MNRAS, 458, 1548
Boro Saikia S., Jeffers S. V., Petit P., Marsden S., Morin J., Folsom C. P., 2015, A&A, 573, A17
Bouvier J., 2008, A&A, 489, L53
Brown T. M., 2014, ApJ, 789, 101
Brown S. F., Donati J.-F., Rees D. E., Semel M., 1991, A&A, 250, 463
Cohen O., Drake J. J., 2014, ApJ, 783, 55
do Nascimento J. D. et al., 2014, in Petit P., Jardine M., Spruit H. C., eds, Proc. IAU Symp. 302, Magnetic Fields throughout Stellar Evolution. Cambridge Univ. Press, Cambridge, p. 142
do Nascimento J.-D., Jr, et al., 2016, ApJ, 820, L15
Donati J.-F., Brown S. F., 1997, A&A, 326, 1135
Donati J.-F., Landstreet J. D., 2009, ARA&A, 47, 333
Donati J.-F. et al., 2003, MNRAS, 345, 1145
Donati J.-F. et al., 2006, MNRAS, 370, 629
Donati J.-F. et al., 2008, MNRAS, 390, 545
Douglas S. T., Agüeros M. A., Covey K. R., Cargile P. A., Barclay T., Cody A., Howell S. B., Kopytova T., 2016, ApJ, 822, 47
Fares R. et al., 2009, MNRAS, 398, 1383
Fares R. et al., 2010, MNRAS, 406, 409
Fares R. et al., 2012, MNRAS, 423, 1006
Fares R., Moutou C., Donati J.-F., Catala C., Shkolnik E. L., Jardine M. M., Cameron A. C., Deleuil M., 2013, MNRAS, 435, 1451
Folsom C. P. et al., 2016, MNRAS, 457, 580
Gallet F., Bouvier J., 2013, A&A, 556, A36
Gallet F., Bouvier J., 2015, A&A, 577, A98
Garraffo C., Drake J. J., Cohen O., 2015, ApJ, 807, L6
Gastine T., Morin J., Duarte L., Reiners A., Christensen U. R., Wicht J., 2013, A&A, 549, L5
Gregory S. G., Jardine M., Collier Cameron A., Donati J.-F., 2006, MNRAS, 373, 827
Gregory S. G., Donati J.-F., Morin J., Hussain G. A. J., Mayne N. J., Hillenbrand L. A., Jardine M., 2012, ApJ, 755, 97
Hébrard É. M., Donati J.-F., Delfosse X., Morin J., Moutou C., Boisse I., 2016, MNRAS, 461, 1465
Irwin J., Bouvier J., 2009, in Mamajek E. E., Soderblom D. R., Wyse R. F. G., eds, Proc. IAU Symp. 258, The Ages of Stars. Cambridge Univ. Press, Cambridge, p. 363
Irwin J., Berta Z. K., Burke C. J., Charbonneau D., Nutzman P., West A. A., Falco E. E., 2011, ApJ, 727, 56
Isobe T., Feigelson E. D., Akritas M. G., Babu G. J., 1990, ApJ, 364, 104
Jardine M., Collier Cameron A., 2008, A&A, 490, 843
Jardine M., Collier Cameron A., Donati J.-F., 2002, MNRAS, 333, 339
Jardine M., Vidotto A. A., See V., 2017, MNRAS, 465, L25
Jeffers S. V., Petit P., Marsden S. C., Morin J., Donati J.-F., Folsom C. P., 2014, A&A, 569, A79
Johnstone C. P., Jardine M., Gregory S. G., Donati J.-F., Hussain G., 2014, MNRAS, 437, 3202
Johnstone C. P., Güdel M., Brott I., Lüftinger T., 2015, A&A, 577, A28
Kitchatinov L. L., Moss D., Sokoloff D., 2014, MNRAS, 442, L1
Koenigl A., 1991, ApJ, 370, L39
Lang P., Jardine M., Donati J.-F., Morin J., Vidotto A., 2012, MNRAS, 424, 1077
Levine R. H., Altschuler M. D., Harvey J. W., 1977, J. Geophys. Res., 82, 1061
Llama J., Vidotto A. A., Jardine M., Wood K., Fares R., Gombosi T. I., 2013, MNRAS, 436, 2179
MacGregor K. B., Brenner M., 1991, ApJ, 376, 204
Marsden S. C. et al., 2014, MNRAS, 444, 3517
Matt S. P., Pinzón G., de la Reza R., Greene T. P., 2010, ApJ, 714, 989
Matt S. P., Pinzón G., Greene T. P., Pudritz R. E., 2012a, ApJ, 745, 101
Matt S. P., MacGregor K. B., Pinsonneault M. H., Greene T. P., 2012b, ApJ, 754, L26 (M12)
Matt S. P., Brun A. S., Baraffe I., Bouvier J., Chabrier G., 2015, ApJ, 799, L23
Meibom S. et al., 2011, ApJ, 733, L9
Meibom S., Barnes S. A., Platais I., Gilliland R. L., Latham D. W., Mathieu R. D., 2015, Nature, 517, 589
Mestel L., Spruit H. C., 1987, MNRAS, 226, 57
Morgenthaler A., Petit P., Morin J., Aurière M., Dintrans B., Konstantinova-Antova R., Marsden S., 2011, Astron. Nachr., 332, 866
Morin J. et al., 2008a, MNRAS, 384, 77
Morin J. et al., 2008b, MNRAS, 390, 567
Morin J., Donati J.-F., Petit P., Delfosse X., Forveille T., Jardine M. M., 2010, MNRAS, 407, 2269
Morin J., Dormy E., Schrinner M., Donati J.-F., 2011, MNRAS, 418, L133
Moutou C., Boisse I., Hébrard G., Hébrard E., Donati J.-F., Delfosse X., Kouach D., 2015, in Martins F., Boissier S., Buat V., Cambrésy L., Petit P., eds, SF2A-2015: Proceedings of the Annual meeting of the French Society of Astronomy and Astrophysics. p. 205
Newton E. R., Irwin J., Charbonneau D., Berta-Thompson Z. K., Dittmann J. A., West A. A., 2016, ApJ, 821, 93
Nicholson B. A. et al., 2016, MNRAS, 459, 1907
Noyes R. W., Hartmann L. W., Baliunas S. L., Duncan D. K., Vaughan A. H., 1984, ApJ, 279, 763
Parker E. N., 1958, ApJ, 128, 664
Petit P. et al., 2008, MNRAS, 388, 80
Pizzolato N., Maggio A., Micela G., Sciortino S., Ventura P., 2003, A&A, 397, 147
Powell K. G., Roe P. L., Linde T. J., Gombosi T. I., De Zeeuw D. L., 1999, J. Comput. Phys., 154, 284
Rebull L. M., Wolff S. C., Strom S. E., 2004, AJ, 127, 1029
Reiners A., Mohanty S., 2012, ApJ, 746, 43
Reiners A., Schüssler M., Passegger V. M., 2014, ApJ, 794, 144
Réville V., Brun A. S., Matt S. P., Strugarek A., Pinto R. F., 2015a, ApJ, 798, 116 (R15)
Réville V., Brun A. S., Strugarek A., Matt S. P., Bouvier J., Folsom C. P., Petit P., 2015b, ApJ, 814, 99
Ribas I. et al., 2016, A&A, 596, A111
Rosén L., Kochukhov O., Hackman T., Lehtinen J., 2016, A&A, 593, A35
See V., Jardine M., Vidotto A. A., Petit P., Marsden S. C., Jeffers S. V., do Nascimento J. D., 2014, A&A, 570, A99
See V., Jardine M., Fares R., Donati J.-F., Moutou C., 2015a, MNRAS, 450, 4323
See V. et al., 2015b, MNRAS, 453, 4301
See V. et al., 2016, MNRAS, 462, 4442
Semel M., 1989, A&A, 225, 456
Spada F., Lanzafame A. C., Lanza A. F., Messina S., Collier Cameron A., 2011, MNRAS, 416, 447
Stauffer J. R. et al., 2016, AJ, 152, 115
van Saders J. L., Pinsonneault M. H., 2013, ApJ, 776, 67
van Saders J. L., Ceillier T., Metcalfe T. S., Silva Aguirre V., Pinsonneault M. H., García R. A., Mathur S., Davies G. R., 2016, Nature, 529, 181
Vidotto A. A., Fares R., Jardine M., Donati J.-F., Opher M., Moutou C., Catala C., Gombosi T. I., 2012, MNRAS, 423, 3285
Vidotto A. A., Jardine M., Morin J., Donati J. F., Opher M., Gombosi T. I., 2014a, MNRAS, 438, 1162
Vidotto A. A. et al., 2014b, MNRAS, 441, 2361
Vidotto A. A., Fares R., Jardine M., Moutou C., Donati J.-F., 2015, MNRAS, 449, 4117
Vidotto A. A. et al., 2016, MNRAS, 455, L52
Wang Y.-M., Sheeley N. R., Jr1990, ApJ, 355, 726
Wang Y.-M., Sheeley N. R., Jr1991, ApJ, 372, L45
Weber E. J., Davis L., Jr1967, ApJ, 148, 217
Wood B. E., 2004, Living Rev. Sol. Phys., 1, 2
Wood B. E., Müller H.-R., Zank G. P., Linsky J. L., Redfield S., 2005, ApJ, 628, L143
Wood B. E., Müller H.-R., Redfield S., Edelman E., 2014, ApJ, 781, L33
Wright N. J., Drake J. J., Mamajek E. E., Henry G. W., 2011, ApJ, 743, 48

This paper has been typeset from a TEX/LATEX file prepared by the author.